Dalton Transactions

Accepted Manuscript

ROYAL SOCIETY OF CHEMISTRY

www.rsc.org/dalton

Facile synthesis and photocatalytic properties of ZnO core/ZnS-CdS solid solution shell nanorods grown vertically on reductive graphene oxide

Jimeng Xu[a], Huanxin Sang[b], Xitao Wang[a], Kang Wang[a]

Corresponding Author, Xitao Wang

Email: wangxt@tju.edu.cn

Address:

[a]Collaborative Innovation Center of Chemical Science and Engineering (Tianjin),

Tianjin Key Laboratory of Applied Catalysis Science and Technology,

College of Chemical Engineering and Technology，

Tianjin University，Tianjin 300072，China

Telephone numbers: 86-022-27402972

[b] Tianjin Academy of Environmental Sciences，Tianjin 300191，China

Abstract

In the present study, ZnS-CdS solid solution sensitized ZnO nanorods were anchored on graphene sheets by combining hydrothermal treatment and ion exchange technique, and the significant influence of CdS content in the shell on photo absorption and photocatalytic performance were investigated. Electron microscopic images reveal that the as-prepared nanocomposites display a sandwich-like 3D structure, consisting of ZnO nanorods with $Zn_xCd_{1-x}S$ or CdS shell grown vertically on both sides of graphene sheets. UV/Vis DRS show that the solid solution sensitized nanocomposites have enhanced visible light absorption and also exhibited a red-shift of the band-edge as compared to RGO/ZnO and RGO/ZnO@ZnS. Fluorescence emission spectra indicate that the deposition of CdS on the shell with appropriate CdS/ZnS ratio and the incorporation of graphene causes improved charge separation. The photocatalytic experiments demonstrate that RGO/ZnO@$Zn_xCd_{1-x}S$ nanocomposites possess much higher photocatalytic activity for H_2 evolution than RGO/ZnO nanorods and RGO/ZnO@ZnS core/shell nanorods. Under the irradiation of 300W Xe lamp, the highest photocatalytic hydrogen production rate of 1865 μmol h^{-1} g^{-1} is observed over RGO/ZnO@$Zn_{0.6}Zn_{0.4}S$ sample, which is about 2.1 and 1.4 times more active than RGO/ZnO and RGO/ZnO@ZnS, respectively. Under the irradiation of visible light (>420 nm), RGO/ZnO and RGO/ZnO@ZnS nanorods are barely active, whereas RGO/ZnO@$Zn_{0.6}Zn_{0.4}S$ displays a hydrogen production rate of 160 μmol h^{-1} g^{-1}. The highly improved performance of the composites can be ascribed to the increased light absorption and efficient charge separation.

Key words: Reductive graphene oxide, ZnO nanorods, $Zn_xCd_{1-x}S$ shell, Photocatalytic H_2 production

Introduction

As a potential solution to coping with energy crisis, environmental pollution and global warming, hydrogen energy is triggering more and more attention. Photocatalytic splitting of water is a promising way to obtain abundant, low-cost hydrogen resource.[1-3] Since TiO_2 was first demonstrated active in photolysis of water by Fujishima and Honda,[4] lots of semiconductors such as metal oxide, metal sulfide and composite have been extensively studied. ZnO, as an important direct wide band gap semiconductor (3.37eV), has drawn attention for photocatalytic application due to its high exciton binding energy (60 meV), rapid generation of photo-excited electron-hole pairs and high photocatalytic activity under UV-light irradiation. But compared to TiO_2, ZnO photocatalyst has some disadvantages such as its low and limited photocatalytic efficiency, easy recombination of electron-hole pair and prone to photocorrosion, which limit its further application. For conquering these drawbacks, Various ZnO-based nanocomposites with different morphologies have been achieved to improve its physical and chemical properties.[5-7] Among these heterostructures, ZnO/ZnS core/shell nanorods have been regarded as a good candidate for photocatalytic H_2 production from water splitting. Although both of ZnO and ZnS are wide bandgap semiconductors, the combination of these two semiconductors could decrease the excited energy and extend the range of light response due to the band alignment between ZnO and ZnS according to their relative energy band locations, resulting in an improved photocatalytic performance for hydrogen production from water splitting as compared to the single phase ZnO or ZnS, whereas the catalysis process is often found to be slow and inefficient for hydrogen production due to the weak absorption in the visible light region and the recombination of photo-generated electron and hole. Thus, further studies are necessary to enhance its photocatalytic performance.

Many investigations have been carried out to improve the photocatalytic efficiency of wide bandgap semiconductor under visible light by coupling low bandgap semiconductor or the incorporation of electron-accepting materials. With coupling nanoscale low-bandgap semiconductor, it can be expected that the photocatalytic activity of ZnO@ZnS core/shell nanorods will be significantly increased by the enhancement of charge separation and photo absorption even under visible light.[8-10] As an important chalcogenide compound, CdS has been used in optical and electronic devices such as photovoltaic cells, photoconductors, infrared (IR) detectors, and superionic conductors. In particular, the low bandgap energy (about 2.3 eV) of CdS increases the capability of absorbing a broad solar spectrum, which makes CdS an effective semiconductor material for photocatalytic application.[11-13] Previous papers showed that various CdS related photocatalytic materials, such as pure CdS,[14, 15] doped CdS,[16, 17] CdS-metallic oxide (TiO_2[18-20] and ZnO[21, 22]), CdS-metal sulfide (ZnS,[23] CuS[24] and Cu_2S[25]), have been prepared. Xin Li and coworkers[20] have synthesized a series of nanostructured TiO_2-CdS composite photocatalysts and analysed influencing factors of pH, molar ratios of starting materials $Na_2S/Cd(NO_3)_2$ and molar ratios of CdS/TiO_2, revealing optimal condition is pH=13.0, the ratio of the starting materials $Na_2S/Cd(NO_3)_2$ closing to 1.0 and molar ratio of CdS/TiO_2 =1:50. Xi Wang and Xiaoyan Li[26] have fabricated layerd CdS/ZnS catalyst film, finding out ZnS outer layer is helpful to restrain the recombination of electron-hole pairs on CdS base layer and enhance the stability of the film and prevent the leaching of Cd^{2+} of the CdS layer. Xi Wang and collaborators[23] have also synthesized heterostructured CdS-ZnS nanoparticles, which ZnS helps to suppress the recombination of electron-hole pairs generated by CdS and improve stability of CdS-ZnS samples.

Furthermore, it has been demonstrated that the combination of active photocatalytic

semiconductors with electron-accepting materials such as graphene oxide (GO) or reduced graphene oxide (RGO) can improve remarkably photocatalytic activity due to effectively suppressing the combination of photogenerated charge carriers. Siqi Liu *et al.*[27] have assembled graphene(GR)-CdS nanocomposites with various weight addition ratios of graphene and the result confirms that introduction of graphene enhances the adsorption capacity of GR-CdS, improves light absorption intensity of visible light region and tunes the microscopic morphology of CdS nanoparticles. Feng Yan[28] and colleagues prepared ZnS-RGO composites *via* a one-pot hydrothermal process, manifesting that the incorporation of RGO increased the specific surface area of ZnS-RGO and helped to hinder electron-hole pair recombination of ZnS. Van Hoang Luan and colleagues[29] have fabricated hybrid 3D structures composed of ZnO nanorods and reduced graphene oxide hydrogel (ZNR-rGOH) through chemical reaction, exhibiting excellent methylene blue removal efficiency. Weijia Han *et al.* [30] have synthesized CdS/ZnO/graphene composite using one-step hydrothermal method, obtaining improved photocatalytic performance too. In addition, the unique two dimensional layer structure of graphene provides a building platform for anchoring vertically other nanostructure such as ZnO nanorods and ZnO/ZnS core/shell nanorods to construct a 3D catalyst system. This kind of photocatalyst possesses many advantages including preventing the aggregation of nanoparticles to enhance surface area and reactive sites in photocatalytic reaction process, increasing the adsorptivity of reactant and facilitating the transfer and separation of charge carriers, which will remarkably improve photocatalytic efficiency over these nanocomposites. Several groups have reported that ZnO nanorods could be vertically grown on the surface of both GO and RGO. The GO films are first deposited on the substrates by spraying or chemical vapor deposition methods, and followed the growth of ZnO nanorods on GO/RGO by hydrothermal

treatment,[31-33] electrochemical deposition[34] or chemical vapor deposition.[35] However, these methods are complicated and need the presence of substrates such as ITO, PET and Si, which obstacle the preparation of catalyst in a large quantity.

Therefore, in present work a facile synthetic method was employed to grow ZnO core/ZnS-CdS solid solution shell nanorods vertically on RGO sheets via combining a hydrothermal growth and liquid-phase chemical conversion. The photocatalytic performance of nanocomposites was evaluated by H_2 production from an alcohol/triethanolamine mixed aqueous solution to illustrate the importance of the structure of sensitized ZnO nanorods grown on RGO sheets and CdS/ZnS molar ratio in the shell for the transportation and separation of photo-generated charges.

2. Experimental

2.1 Materials

All chemical reagents were of analytical grade and used without further purification. Graphene oxide was prepared from strengthened Hummers method.[36, 37]

2.1.1 Preparation of ZnO nanorods grown on RGO

30 mL ethanol solution of $Zn(CH_3COO)_2$ (0.167 $mol \cdot L^{-1}$) was added slowly to a 20 mL GO solution (8 $mg \cdot mL^{-1}$) while stirring, and the mixture was heated in a water bath at 90 ^oC to evaporate solvent under magnetic stirring. Then, the sample was calcined at 375 ^oC for 1 h in a N_2 atmosphere to obtain ZnO seed layers on graphene sheets.

The as-prepared RGO/ZnO seed layer was dispersed in 80 mL aqueous solution of PVP (2.5 $mg \cdot mL^{-1}$) under ultrasonication for 2 h, which is cooled to 0^oC in a ice-water bath, then 1.5 g zinc nitrate was added in this solution. After keeping for 2.5 h at 0^oC, 5 $mol \cdot L^{-1}$ NaOH solution was added drop by drop to adjust pH to ~14, the mixture was allowed to react at 60 ^oC in a bath for 5 h.

The sample was transfered into a Teflon-lined stainless steel autoclave. Subsequently, the autoclave was kept at 180 ^{o}C for 36 h as reported before[38] and cooled down to room temperature. The black precipitate was collected after centrifugal separation. Finally, the product was washed with deionized water and absolute ethanol for three times, respectively and drying at 60 ^{o}C over night, which was marked as RGO/ZnO.

2.1.2 Preparation of ZnO@ZnS core/shell nanorods grown on RGO

0.1 g as-prepared RGO/ZnO nanorods were dispersed in 20 mL deionized water, and 50 mL Na_2S (0.05 g, 0.2 mmol) solution was added dropwise under ultrasonication for 0.5 h, then the mixture was heated at 70 ^{o}C for 5 h[39] under magnetic stirring. The obtained product was washed with absolute ethanol and water three times and dried at 60 ^{o}C over night, which is marked as RGO/ZnO@ZnS.

2.1.3 Preparation of CdS-sensitized ZnO@ZnS nanorods grown on RGO

As-prepared RGO/ZnO@ZnS sample was dispersed in 20 mL deionized water under ultrasonication for 0.5 h, then 40 mL $Cd(NO_3)_2$ solution was added into above mixture. The sample was transferred into a Teflon bottle and heated at 180 ^{o}C for 12 h. After the reaction, the resultant sample was washed with deionized water and absolute ethanol three times, respectively and dried at 60 ^{o}C overnight. By means of changing the concentration of $Cd(NO_3)_2$ solution, three RGO/ZnO@$Zn_xCd_{1-x}S$ samples with different conversion ratios of ZnS to CdS (0.1, 0.4 and 1) were prepared, marked as RGO/ZnO@$Zn_{0.9}Cd_{0.1}S$, RGO/ZnO@$Zn_{0.6}Cd_{0.4}S$ and RGO/ZnO@CdS, respectively.

2.2 Characterization

The morphologies of samples were characterized by a Hitachi S-4800 scanning electron

microscope (SEM, 5 kV). Transmission electron microscopy (TEM) and higher-magnification transmission electron microscopy (HRTEM) were obtained with JEOL-2100F system (200 kV). Specimens for TEM and HRTEM measurements were prepared via drop-casting a droplet of ethanol suspension onto a copper grid, coated with a thin layer of amorphous carbon film, and dried in air.

XRD patterns of composites were confirmed by a D/MAX-2500 automatic powder diffractometer equipped with Cu Kα radiation flux (λ=0.15418) at a scanning rate of 0.02 s^{-1} in the 2θ range of 15~80°.

Ultraviolet and visible diffusive reflectance spectra (UV-Vis DRS) were taken on an UV-Vis spectrometer (Perkin Elmer, Lambda 750), the scanned range being 200-800 nm against barium sulfate standard.

Raman spectra were executed on a DXR Raman microscope (Thermo Scientific, American) using a 325 nm high brightness laser excitation.

Photoluminescence (PL) spectra were tested through using a Fluorolog 3 photoluminescence spectrometer (Horiba Jobin Yvon, Japan). The spectra were obtained in range of 400~680 nm using a 325 nm laser excitation.

Photoelectrochemical measurements were performed in an electrochemistry workstation (CHI 660, CH Instrument, Austin, TX) with a three-electrode system using a three-compartment glass cell. The working electrode was obtained by drop-casting a drop of as-prepared products on FTO electrode. A platinum plate and a saturated calomel electrode (SCE) were used as the counter electrode and reference electrode, respectively. If not specified, all potentials were recorded according to saturated calomel electrode (SCE) in this study. The experiments were operated at

room temperature with 0.25M Na_2S and 0.15M Na_2SO_3 mixted solution as electrolyte.

2.3 photocatalytic test

The photocatalytic performance of the samples was evaluated by H_2 production from a mixed solution of 100 mL H_2O, 50 mL CH_3CH_2OH and 2mL $N(CH_2CH_3)_3$ under a 300W Xenon lamp(PLS-SXE300C, Beijing Perfectlight Co., Ltd. , emitting in the 320-1100 nm wavelength range) in a tank reactor equipped with a top quartz glass with diameter of 5cm. In a typical experiment, 25 mg of photocatalyst was suspended in solution under magnetic stirring. The temperature of the solution was maintained at room temperature by a flow of cooling water. Prior to the irradiation, the photocatalytic reaction system was flushed with an Argon flow of 30 mL/min for 2h to remove the air in the reactor, then an Argon flow of 5 mL/min was used as a carrier gas through the reactor to the analysis system. The products of the reaction were analyzed by an on-line gas chromatography using thermal conductivity detector (Agilent 4890, nitrogen as a carrier gas).

The hydrogen production rate is calculated as following formula.

$$H_2(\mu mol\ h^{-1}\ g^{-1}) = \frac{H_2\ \%\ (v/v)\ \times\ flow\ rate\ (mL\ h^{-1})}{22414\ (mL\ mol^{-1})\ \times\ m_c\ (g)}$$

The apparent quantum efficiency (QE) was measured under the same photocatalytic reaction conditions. The QE was calculated by following formula.

$$QE(\%) = \frac{number\ of\ reacted\ electrons}{number\ of\ incident\ photons} \times 100$$
$$= \frac{number\ of\ evolved\ H_2\ molecules \times 2}{number\ of\ incident\ photons} \times 100$$

3. Results and discussion

3.1 Morphology, composition and structure of nanocomposites

The fabrication of the nanocomposites is depicted in Figure 1 a. Firstly, ZnO seed layer on graphene was prepared via an impregnation-calcination method, and then ZnO nanorods were

grown on the surface of the RGO by hydrothermal reaction of RGO/ZnO seeds. Secondly, RGO/ZnO@ZnS core-shell nanorods were synthesized by anion exchange reaction of RGO/ZnO nanorods with Na_2S solution. Finally, RGO/ZnO@$Zn_xCd_{1-x}S$ core-shell nanorods are obtained by cation exchange reaction of RGO/ZnO@ZnS with $Cd(NO_3)_2$ solution.

As shown in Fig. 1 (b), (c), (d) and (e), RGO/ZnO sample displays a sandwich-like ZnO nanorods/RGO/ZnO nanorods heterostructures, and the uniform nanorods with estimated length of 200 ~ 300 nm and diameter of 20~40 nm were grown vertically on both sides of graphene sheets. After the deposition of ZnS (Fig. 1 (f) and (g)), the surface of the ZnO nanorods became rougher and thicker, indicating the conversion of ZnO nanorod to ZnO/ZnS core/shell structure via the surface sulfidation. EDS (energy dispersive spectrometer) spectrum of the RGO/ZnO@ZnS in Fig. 1 (g) inset reveals the existence of C, O, S and Zn elements, further confirming the formation of ZnS shell.

When RGO/ZnO@ZnS nanorods were immersed in $Cd(NO_3)_2$ solution under hydrothermal condition, cation exchange began at the interfaces between the ZnS shell layer surfaces and $Cd(NO_3)_2$ solution. With the increase in the concentration of $Cd(NO_3)_2$, ZnS was gradually substituted by CdS, resulting in a ZnS-CdS solid solution shell layer. The conversion dynamic of single component shell to bi-component shell comes from the difference in solubility-product constant (K_{sp}) between ZnS ($K_{sp} = 2.93\times10^{-25}$) and CdS ($K_{sp} = 8.0\times10^{-27}$). The TEM images in Fig. 1(h), (j) and (l) show the structure of core/shell nanorods anchored on graphene sheets maintains unchanged after the conversion. Moreover, HRTEM images taken from the edge of rods in Fig. 1(i), (k) and (m) confirm further the formation of $Zn_xCd_{1-x}S$ shell. The interplanar spacings of 0.317 nm, 0.328 nm and 0.338 nm corresponded well to the spacing between the (111) planes of reference wurtzite ZnS(0.31 nm) and wurtzite CdS(0.34 nm), which was in good accordance with the previous study of $Zn_xCd_{1-x}S$ solid solution,[40, 41] indicating the Cd^{2+} incorporated into the ZnS

lattices and the formation of $Zn_xCd_{1-x}S$ solid solution.

The EDS of RGO/ZnO@$Zn_{0.6}Cd_{0.4}S$ in the inset of Fig.1(j) demonstrates the existence of Zn, O, C, Cd and S, also confirming the successful incorporation of Cd into RGO/ZnO@ZnS system through cation exchange. Furthermore, the line scanning spectroscopy of RGO/ZnO@CdS sample in the inset of Fig.1(l) shows that the distribution curves of Cd and S elements appear an "m" shape, while those for Zn and O elements are n-like shape, illustrating that Cd and S elements are mainly accumulated in the shell of nanorod and the core of nanorod is ZnO.

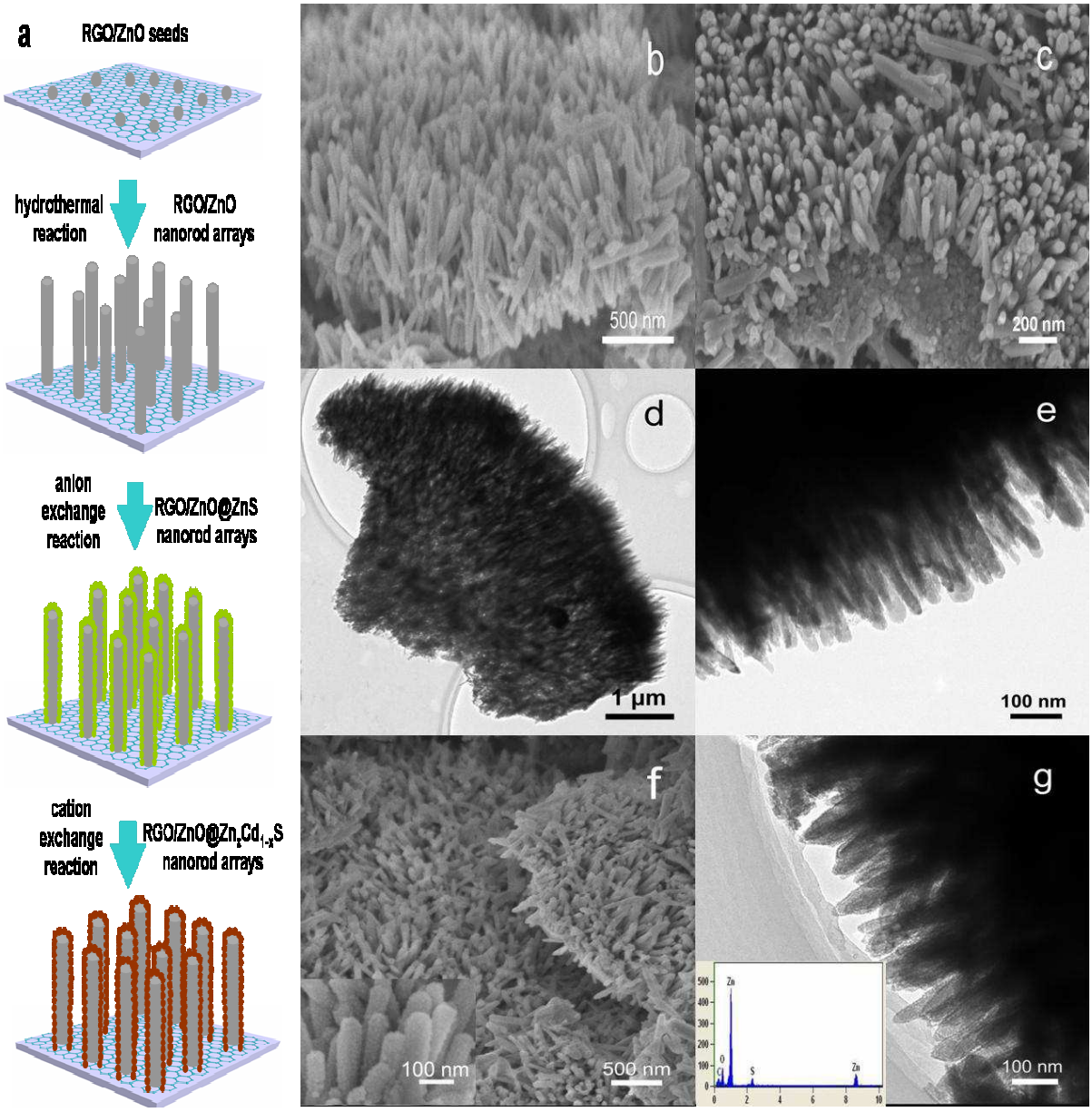

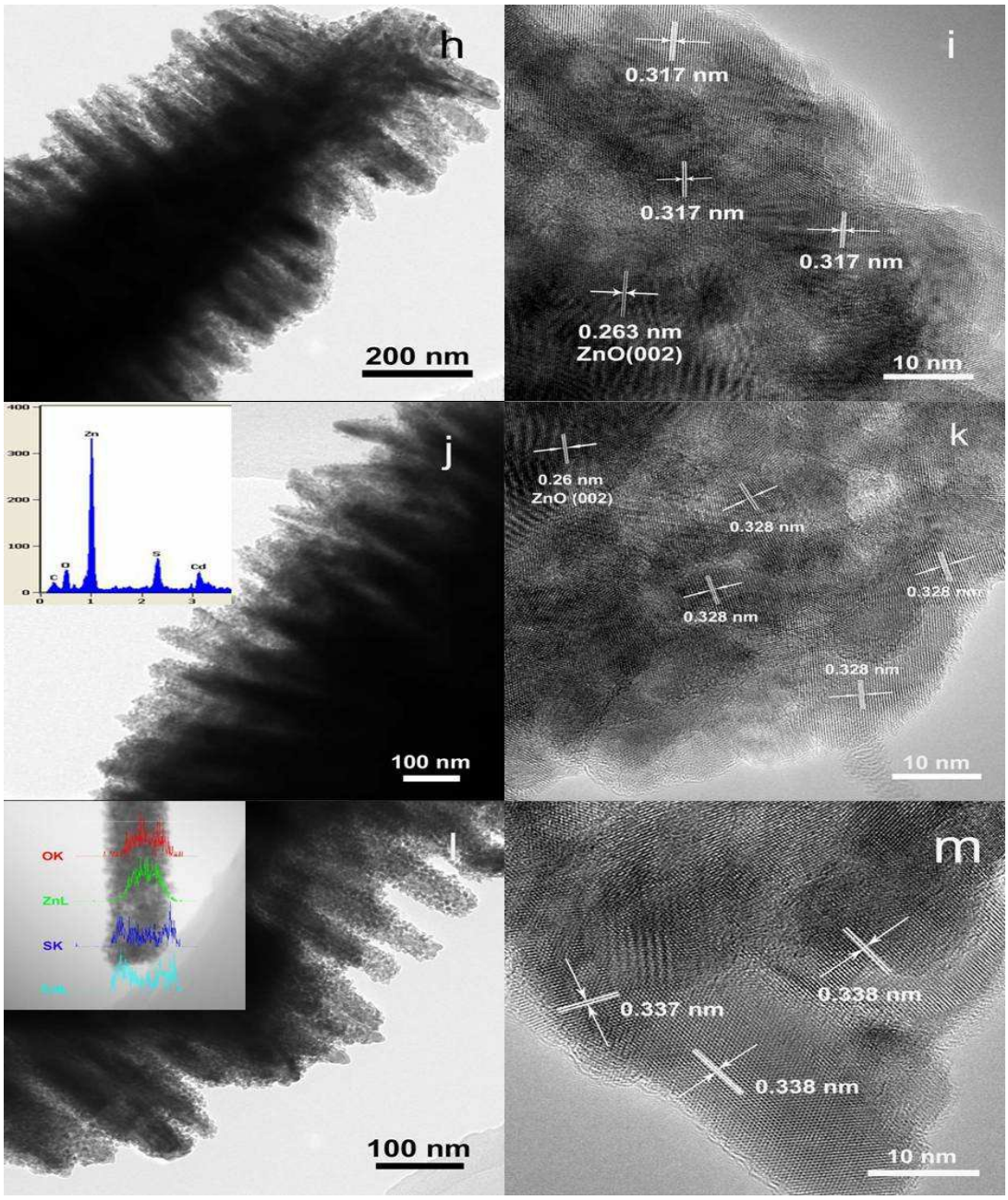

Fig. 1 schematic diagram of the preparation process (a) and SEM, TEM and HRTEM images of (b, c, d and e) RGO/ZnO; (f, g) RGO/ZnO@ZnS; (h, i) RGO/ZnO@$Zn_{0.9}Cd_{0.1}S$; (j, k) RGO/ZnO@$Zn_{0.6}Cd_{0.4}S$; (l, m) RGO/ZnO@CdS.

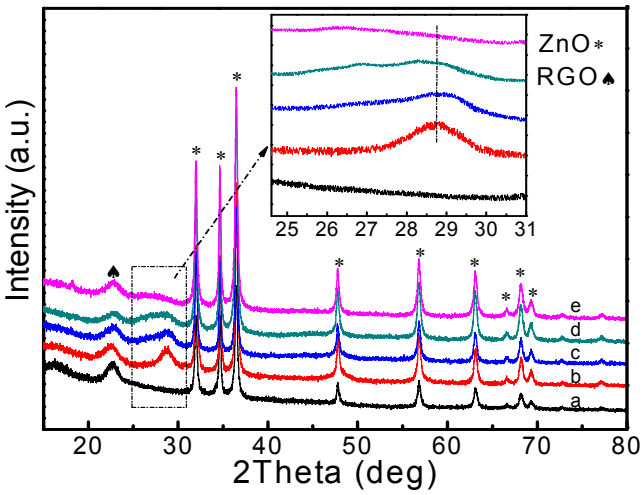

Fig. 2 XRD patterns of (a)RGO/ZnO; (b)RGO/ZnO@ZnS; (c) RGO/ZnO@$Zn_{0.9}Cd_{0.1}S$; (d)RGO/ZnO@$Zn_{0.6}Cd_{0.4}S$; (e)RGO/ZnO@CdS;

The crystal composition and microstructure of as-prepared nanocomposites was analyzed by X-ray diffraction (XRD). It can be seen clearly that all patterns exhibit 9 characteristic peaks corresponding to hexagonal ZnO (JCPDS36-1451) and one at 2θ=22.9° ascribed to reductive graphene oxide,[42, 43] suggesting the existence of ZnO core part and the reduction of GO to RGO during the preparation. Meanwhile, a broadening peak at 2θ=28.62° for RGO/ZnO@ZnS (curve b) is detected, which matches well with the face-centered-cubic ZnS (JCPDS65-0309), confirming the conversion of ZnO nanorods to ZnO@ZnS core/shell nanorods. Because the peaks at 2θ=47.83° of (220) and 2θ=56.76° of (311) crystal plane of ZnS are very close to the diffraction peaks of (102) and (101) crystal plane of ZnO, these two peaks are overlapped together, respectively. The magnified patterns in Fig. 2 reveal that the diffraction peak related to ZnS in Cd-containing nanocomposites shifts gradually to small angle with the increase of Cd loading. [44, 45] This result suggests that Cd^{2+} is incorporated into ZnS lattice and $Zn_xCd_{1-x}S$ solid solution is formed, which agrees with the HRTEM images.

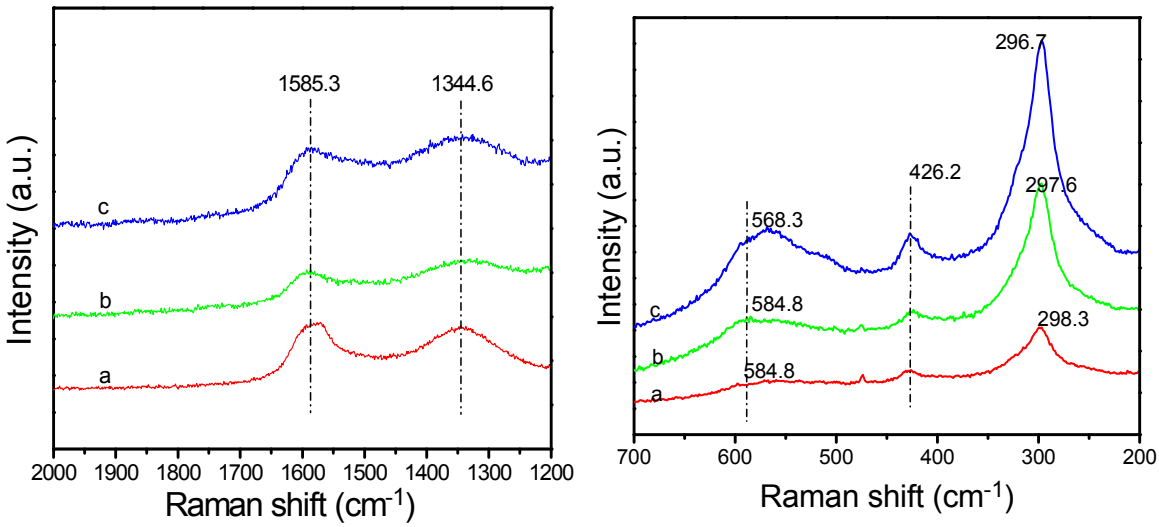

Fig.3 Raman spectra of RGO/ZnO@$Zn_{0.9}Cd_{0.1}S$(a), RGO/ZnO@$Zn_{0.6}Cd_{0.4}S$(b) and RGO/ZnO@CdS(c) nanocomposites

In order to confirm the phase structure of ZnS and CdS on the surface of ZnO nanorods, Raman measurements were employed to investigate the composition of nanocomposites. Fig. 3 displays Raman spectra of CdS-sensitized nanocomposites. Two vibration peaks at ~1344.6 cm^{-1} and ~1585.3 cm^{-1} [46] were found for all Raman spectra, which can be assigned to D band and G band respectively, well-known features of carbon materials in Raman spectra, indicating the presence of RGO. The peak at 426.2 cm^{-1} is ascribed to ZnO non-polar optical phonons E2 mode, which is a typical of ZnO Raman active branches.[47] In addition, a strong peak at around 298 nm and a weak peak at around 584.8 nm assigned to the 1-LO and 2-LO phonon modes of CdS are detected, which is a direct evidence for the conversion of ZnS to CdS. The relative intensities of both 1-LO and 2-LO peaks obviously became stronger due to the increase of CdS content in the shell. Also, these two peaks shifted continuously to higher frequencies with increasing CdS content, suggesting an alloy system of $Zn_xCd_{1-x}S$ in contrast to a mixture of separate CdS and ZnS phases, where no peak position shifts are expected with varying stoichiometry.[48, 49] The Raman-active SO (surface optical)

phonon mode of ZnS around 324.3 cm^{-1} is overlapped together with Raman peak of CdS.

3.2 optical properties of RGO/ZnO@$Zn_xCd_{1-x}S$ nanocomposites

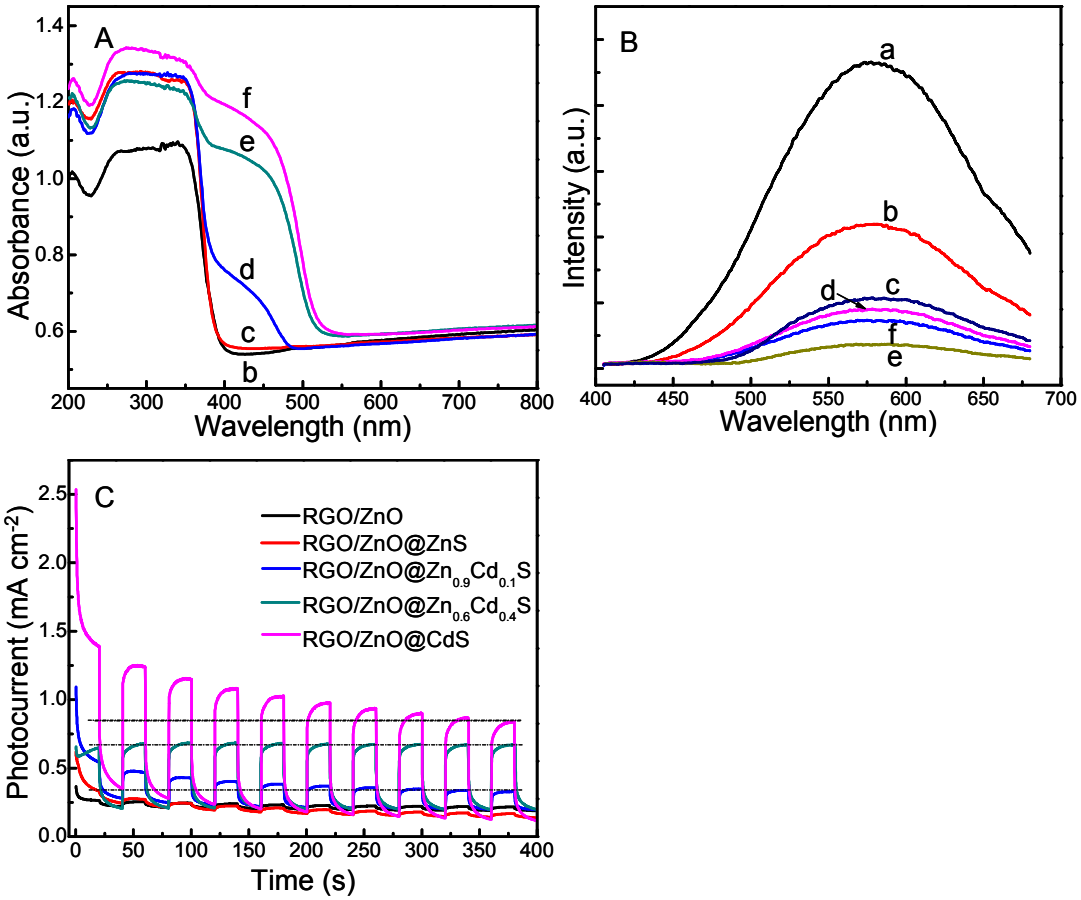

Fig. 4 (A) UV-Vis DRS, (B) Room-temperature PL spectra of (a) ZnO nanorods; (b) RGO/ZnO; (c)RGO/ZnO@ZnS; (d)RGO/ZnO@$Zn_{0.9}Cd_{0.1}S$; (e)RGO/ZnO@$Zn_{0.6}Cd_{0.4}S$; (f)RGO/ZnO@CdS and (C) photocurrent response of nanocomposites.

The UV-vis absorption spectra of the as-prepared RGO/ZnO@$Zn_xCd_{1-x}S$ nanocomposites with different CdS content, together with RGO/ZnO and RGO/ZnO@ZnS for comparison are shown in Fig.4 A. The strong characteristic absorption below 400nm for all samples indicates the existence of highly crystalline ZnO. Similar to RGO/ZnO sample, RGO/ZnO@ZnS displays a strong absorption in the range of UV light and weak visible absorption due to the wide band gap of ZnS. After the deposition of Cd, obvious red shifts of the photo absorption edges are seen, which is due to the

incorporation of CdS with narrow band gap and the formation of $Zn_xCd_{1-x}S$ solid solution. The nanocomposites show good absorption in the visible region (λ=400-520 nm), suggesting these samples might exhibit good photocatalytic behaviors under visible light. Moreover, the absorption of the RGO/ZnO@$Zn_xCd_{1-x}S$ samples in the visible region become stronger with increasing of the $Cd(NO_3)_2$ concentration, indicating the increase of Cd content in the shell. However, the increasing scope of photo absorption decreases rapidly when conversion ratio of ZnS changing from 0.4 to 1, showing further increase in Cd loading cannot improve the photo absorption of RGO/ZnO@ $Zn_xCd_{1-x}S$ remarkably. According to previous paper[50], the bandgap value of $Zn_xCd_{1-x}S$ architectures can be estimated through extrapolating the linear part of the (hv) - $(\alpha hv)^2$ to $(\alpha hv)^2 = 0$, where α is the absorption coefficient, hv is the discrete photon energy. The estimated E_g values of $Zn_xCd_{1-x}S$ are shown in Table 1; they show a gradual reduction with increasing Cd content.

Room-temperature PL spectra of RGO/ZnO@ $Zn_xCd_{1-x}S$ series, ZnO nanorods, RGO/ZnO and RGO/ZnO@ZnS nanorods are shown in Fig.4 B. All sample exhibit a broad fluorescence emission at the range of 400-700 nm, which are generally believed coming from the surface defects of ZnO.[51] It is evident that the ZnO nanorods possess the strongest fluorescence emission peak among these composites, implying the fastest combination rate of photogenerated electrons and holes. After the addition of graphene, fluorescence emission intensity of RGO/ZnO decreases dramatically. This phenomenon suggests that the RGO/ZnO nanocomposites have a lower recombination rate of electrons and holes, which is the fact that graphene is a good electron acceptor with great electronic transmission capacity and the electrons are excited from the valence band of ZnO nanorods to the conduction band and then transfer to graphene sheets, preventing a direct recombination of electrons and holes. After the conversion of RGO/ZnO nanorods to

RGO/ZnO@ZnS and RGO/ZnO@$Zn_xCd_{1-x}S$ core-shell nanorods, further decrease of fluorescence emission is observed, indicating that the recombination of photo-generated carriers was effectively suppressed due to the composite effect of semiconductors. In addition, the emission intensity of RGO/ZnO@$Zn_xCd_{1-x}S$ decreases first with the increase of Cd content, then increase with the further increase of that, which indicates that there is an optimum molar ratio of CdS/ZnS for suppressing the recombination of photo-generated carriers. The increase of recombination rate of electrons and holes over RGO/ZnO@CdS nanocomposites can be due to the formation of larger particles and thicker layer of CdS, in which photo-generated holes and electrons would more easily recombine.

To provide an additional evidence for the above suggested observation, the transient photocurrent responses of RGO/ZnO, RGO/ZnO@ZnS and RGO/ZnO@$Zn_xCd_{1-x}S$ series were recorded for several on-off cycles under visible light (>420 nm). Fig. 4 C shows the photocurrent-time curves for all samples. As can be seen from figure, nanocomposites containing Cd exhibit much higher photocurrents as compared to RGO/ZnO and RGO/ZnO@ZnS, and the photocurrent increases gradually with the increase of the Cd content. This enhancement could be attributed to the improved photo absorption in the range of visible light arising from the addition of Cd. It is worthy to note that the photocurrent of the RGO/ZnO@$Zn_{0.9}Cd_{0.1}S$ and RGO/ZnO@CdS decreased obviously with irradiation time. Their initial photocurrent of ~1.1 mA/cm^2 and ~2.5 mA/cm^2 decayed to 0.32 mA/cm^2 and 0.84 mA/cm^2 after 10 cycles, respectively. It is proposed that the continuous decay could be due to the gradual photocorrosion of CdS. In contrast to those two composites, RGO/ZnO@$Zn_{0.9}Cd_{0.1}S$ sample shows much steadier photocurrent, which almost maintains unchanged (0.68 mA/cm^2). The steady photocurrent reveals that the photocorrosion of CdS can be prevented by adjusting the molar ratio of CdS/ZnS and the formation of $Zn_xCd_{1-x}S$ solid

solution in the shell. This result should be related to coupling effects and the chemical interaction between CdS and ZnS. Too high or too low CdS/ZnS ratio must decrease the amount of heterojunction between ZnS and CdS, resulting in a weak chemical interaction and slow transfer of photogenerated charge carriers.

3.3 Photocatalytic activity

The photocatalytic performances of all nanocomposites were evaluated by the rates of the photocatalytic H_2 production from trithylamine/alcohol aqueous solution under irradiation of Xenon lamp (300W). Typical results obtained are shown in Fig. 5, where the rates of hydrogen production are plotted as functions of irradiation time. Obviously, the rates of hydrogen production on all the catalysts reach a maximum at ca. 1.5-2.5 h and then show a steady state even after 5 hours' prolonged irradiation. This plateau can be related to the concentration of intermediate product from the partial dehydrogenation/oxidation of ethanol and triethanolamine. Among these catalysts, the RGO/ZnO nanorods exhibit the lowest photocatalytic activity (610 μmol g^{-1} h^{-1}) due to the weak photo absorption. After the deposition of the ZnS nanoparticles on the surface of the ZnO nanorods, the hydrogen yields are improved slightly (790 μmol g^{-1} h^{-1}) because of the coupling effect of semiconductors. Fig. 5 A also shows the effects of Cd content on the photocatalytic activity of the RGO/ZnO@ZnS nanorods. All Cd containing composites display a photocatalytic H_2 evolution rate much higher than that of RGO/ZnO@ZnS, revealing addition of Cd in the shell affects greatly the photocatalytic activity of RGO/ZnO@ZnS nanorods. The rate of the photocatalytic H_2 production initially increases with an increase of Cd content in the shell, and then it decreases with further increase of Cd amount. The RGO/ZnO@$Zn_{0.6}Cd_{0.4}S$ sample exhibits a maximum H_2 production rate of 1865 μmol h^{-1} g^{-1}, which is about 3.1 and 2.4 times more active than RGO/ZnO and

RGO/ZnO@ZnS, respectively, and the apparent quantum efficiency of 22.6% can be obtained. Moreover, the photocatalytic activity of RGO/ZnO@$Zn_{0.6}Cd_{0.4}S$ under irradiation of visible light (>420 nm) was evaluated compared to that of RGO/ZnO and RGO/ZnO@ZnS samples, as shown in Fig. 5 B. It can be seen that RGO/ZnO and RGO/ZnO@ZnS samples show barely active for H_2 production under visible light, which can be due to the weak visible light response of these both samples. However, RGO/ZnO@$Zn_{0.6}Cd_{0.4}S$ has a photocatalytic H_2 production rate of ~160 μmol g^{-1} h^{-1}, suggesting the significant influence of Cd on photocatalytic activity.

According to the discussion on characterizations mentioned above, RGO/ZnO@$Zn_{0.6}Cd_{0.4}S$ nanorods with a proper CdS/ZnS molar ratio and thickness of shell layer in the shell has more heterojunction between ZnS and CdS compared to the other two samples, which favours the separation and transfer of photoinduced charge carriers, finally inhibiting the recombination of charge carriers and photocorrosion of CdS. The decrease in photocatalytic performance of the RGO/ZnO@CdS sample can be attributed to the agglomeration of CdS into larger particles, thicker CdS layer in the shell and the decrease of heterojunction between ZnS and CdS, which in turn results in an increase in recombination rate of photo-generated electrons and holes.

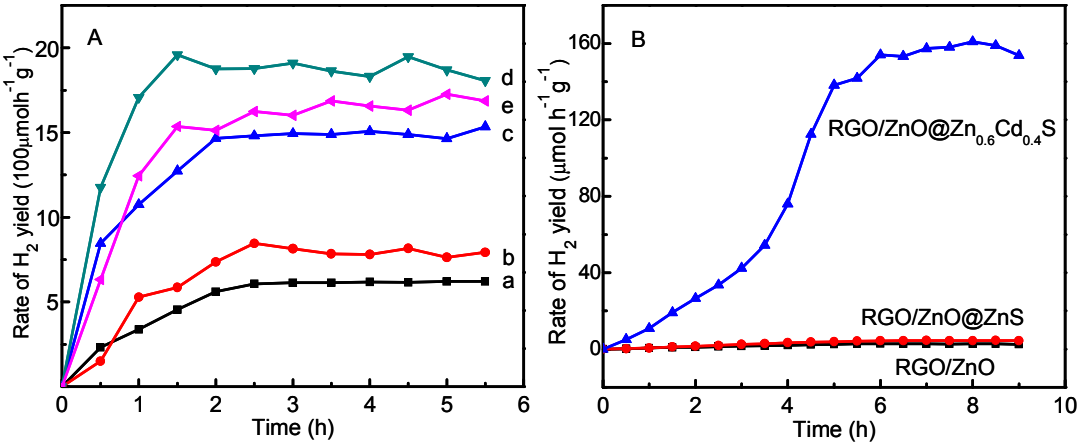

Fig.5 (A) Rates of the photocatalytic H_2 production from trithylamine alcohol aqueous solution

under the irradiation of 300W Xe lamp. (a) RGO/ZnO, (b) RGO/ZnO@ZnS, (c) RGO/ZnO@$Zn_{0.9}Cd_{0.1}S$, (d) RGO/ZnO@$Zn_{0.6}Cd_{0.4}S$, (e) RGO/ZnO@CdS; (B) Rates of the photocatalytic H_2 production from trithylamine alcohol aqueous solution under the irradiation of 300W Xe lamp with a cut-off filter (>420 nm)

3.4 Photocatalytic activity enhancement mechanism of RGO/ZnO@$Zn_xCd_{1-x}S$ samples

The enhanced photocatalytic activity over CdS containing composites is mainly related to the superior photo absorption in the visible region and the efficient generation, separation and transfer process of the photoinduced electron-hole pairs, which strongly depends on the band structure of the composites. Thus, the valence band (VB) edge positions and the conduction band (CB) edge positions of ZnO, ZnS, CdS and $Zn_xCd_{1-x}S$ composites were estimated according to the following empirical formula[52, 53]

$$E_{VB} = X - E^e + 0.5E_g \quad (1)$$

$$E_{CB} = E_{VB} - E_g \quad (2)$$

Where E_{VB} is the VB edge potential, X is the electronegativity of semiconductor that is geometric mean of electronegativity of constituent atoms, E^e is the energy of free electrons on the hydrogen scale (~4.5 eV), E_g is the band gap energy of the semiconductor and E_{CB} is the CB edge potential. Using values of X and E_g in table 1 and formula (1) and (2), E_{VB} and E_{CB} values of ZnO, ZnS, CdS and $Zn_xCd_{1-x}S$ composites were counted and listed in Table 1.

Table 1 the VB edge positions and CB edge positions of ZnO, ZnS, CdS and $Zn_xCd_{1-x}S$ composites estimated by empirical formula

Semiconductor	X (eV)	E_g [a] (eV)	E_{VB} (eV)	E_{CB} (eV)
ZnO	5.790	3.0	2.90	-0.32
ZnS	5.265	3.11	2.48	-0.95

$Zn_{0.9}Cd_{0.1}S$	5.25	3.01	2.26	-0.75
$Zn_{0.6}Cd_{0.4}S$	5.23	2.25	1.86	-0.39
CdS	5.180	2.19	1.78	-0.41

According to E_{VB} and E_{CB} values in Table 1 and the reported work function of graphene (-0.08eV *vs.* NHE),[54] the possible charge transfer process over RGO/ZnO@$Zn_xCd_{1-x}S$ is shown in Fig. 6. For three Cd-containing composites, the electrons in VB edge could be excited to conduction band and these electrons could easily shift to ZnO and RGO in turn, leaving holes on the valence band. Hence, the photogenerated electrons and holes were separated efficiently. The electrons in the graphene (-0.08 eV) could reduce H_2O to H_2 because of slightly higher potential than H_2/H^+. Meanwhile, the photogenerated holes at the VB top of $Zn_xCd_{1-x}S$ would immediately oxidize trithylamine and ethanol to the final product. These efficient-separated electrons and holes generating under visible light over CdS-containing samples would explain why RGO/ZnO@$Zn_xCd_{1-x}S$ series have higher photocatalytic activity than RGO/ZnO and RGO/ZnO@ZnS. Due to the low absorption under visible light and photocorrosion of sulfide resulting from the small CdS loading, RGO/ZnO@$Zn_{0.9}Cd_{0.1}S$ exhibits the lowest hydrogen production rate among these three nanocomposites. However, excessive amount of CdS also decreases the photocatalytic activity over RGO/ZnO@CdS as compared to RGO/ZnO@$Zn_{0.6}Cd_{0.4}S$ because of the agglomerate of CdS and thicker CdS layer, leading to photogenerated electrons and holes more easily to recombine on surface of CdS. In addition, the photocorrosion of CdS in RGO/ZnO@CdS sample will be another important reason for inferior photocatalytic performance.

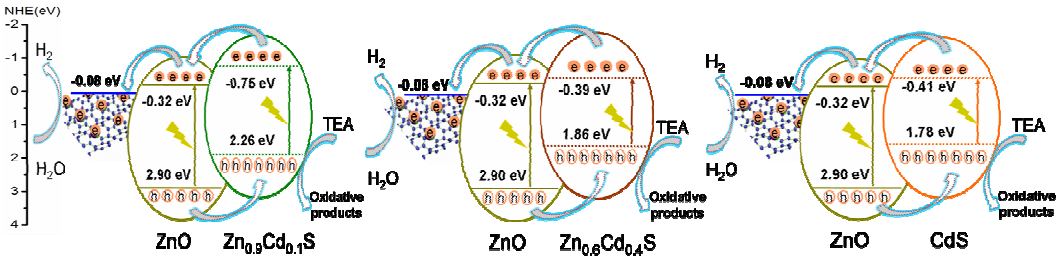

Fig.6 schematic diagram for the charge-transfer process in RGO/ZnO@$Zn_xCd_{1-x}S$ nanocomposites

4. Conclusions

The nanocomposites of RGO/ZnO@$Zn_xCd_{1-x}S$ with different CdS/ZnS molar ratios were successfully synthesized by combining the hydrothermal process and ion exchange technique. The as-prepared composite photocatalysts exhibit a sandwich-like 3 D heterostructure by growing ZnO@$Zn_xCd_{1-x}S$ core/shell nanorods on both sides of graphene sheets. These Cd-containing compostites exhibit enhanced photo absorption and photocatalytic activities in photocatalytic H_2 production from trithylamine alcohol aqueous solution under the irradiation of Xe lamp or visible light. Under the optimal Cd content, the highest photocatalytic hydrogen production rates of 1865 μmol g^{-1} h^{-1} under the irradiation of Xe lamp and of ~160 μmol g^{-1} h^{-1} under visible light are obtained, respectively. The highly improved performance of the composites can be ascribed to the increased light absorption and efficient charge separation.

Acknowledgements

We gratefully acknowledge the financial support from the National Natural Science Foundation of China (No. 21276190 and 20806059).

References

[1] Best, James P., Dunstan, Dave E. *International Journal of hydrogen energy*, 2009, 34(18), 7562-7578.

[2] Kothari R, Buddhi D, Sawhney RL. *Renew Sustain Energy Rev*, 2008, 12, 553-563.

[3] Osterloh, Frank E. *Chemistry of Materials*, 2008, 20(1), 35-54.

[4] Fujishima A, Honda K. *Nature*, 1972, 238, 37-38.

[5] J. J. Wu, C.H. Tseng. *Applied Catalysis B: Environmental*, 2006, 26, 51-57.

[6] K. Liu, J. Zhang, H. Gao, T. Xie, D. Wang. *Journal of Alloys and Compounds*, 2013, 552, 229-303.

[7] F. Xu, Y. Yuan, H. Han, D. Wu, Z. Gao and K. Jiang. *Crys.tEng.Comm.*, 2012, 14, 3615-3622.

[8] W. Lia, G. Song, F. Xie, M. Chen and Y. Zhao, *Mater. Lett.*, 2013, 96, 221-223.

[9] L.Yu, W. Chen, D. Li, J. Wang, Y. Shao, M. He, P. Wang, X. Zhen. *Applied Catalysis B-Environmental*, 2014, 164, 453-461.

[10] W. Zhang, S. Wang, Y. Wang, Z. Zhu, X. Gao, J.Yang, H. Zhang. *RSC Advances*, 2015, 5(4), 2620-2629.

[11] S. Li, W. Zhu, Y. Xue, S. Liu. *Biosensors & bioelectronics*, 2014, 64, 611-617.

[12] M. S. Kumar, D. A. Kumar, D. Supriyam, Srivastava Divesh N., Paul Parimal, Mondal Anup, Adhilary Bibhutosh. *Applied Catalysis B-environmental*, 2014, 163, 628-628.

[13] J. Xu, X. Cao. *Chemical Engineering Journal*, 2014, 260, 642-648.

[14] B. Kaboudin, F. Kazemi, A. Ghaderian, Z. Zand. *Journal of the Iranian Chemical Society*, 2014, 11, 1121-1127.

[15] Samantha A. L. Bastos Paula A. L. Lopes, Fábio N. Santos, L. A. Silva. *International Journal of Hydrogen Energy*, 2014, 39, 14588-14595.

[16] X. Li, H. Wang, T. Chu, D. Li, L. Mao. *Materials Research Bulletin*，2014, 57, 254-259.

[17] A Daya Mani, N Xanthopoulos, Danielelaub, C H Subrahmanyam. *J. Chem. Sci*，2014, 126 (4), 967-973.

[18] Z. Xie, X. Liu, W. Wang, C. Liu, Z. Li, Z. Zhang. *Science and Technology of Advanced Materials*, 2014, 15.

[19] B. Pant, H. R. Pant, M. Park, Y. Liu, J. W. Choi, Nasser A.M. Barakat, H. Y. Kim. *Catalysis Communications*, 2014, 50, 63-68.

[20] X. Li, T. Xia, C. Xu, James M., X. Chen. *Catalysis Today*, 2014, 225, 64-73.

[21] M. H. Habibi, M. H. Rahmati. *Spectrochimica Acta Part A: Molecular and Biomolecular Spectroscopy*, 2015, 137, 160-164.

[22] W. Han, L. Ren, X. Qi, Y. Liu, X. Wei, Z. Huang, J. Zhong. *Applied Surface Science*, 2014, 299, 12-18.

[23] X. Wang, W. Peng, X. Li. *International Journal of Hydrogen energy*, 2014, 39, 13454-13461.

[24] E. Hong, D. Kim, J. H. Kim. *Journal of Industrial and Engineering Chemistry*, 2014, 20, 3869-3874.

[25] Ilan Jen-La Plante, Ayelet Teitelboim, Iddo Pinkas, Dan Oron, and Taleb Mokari. *The Journal of Physical Chemistry Letters*, 2014, 5, 590-596.

[26] X. Wang, X. Li. *Material Science and Engineering B*, 2014, 181, 86-92.

[27] S. Liu, M. Yang, N. Zhang, Y. Xu. *Journal of energy Chemistry*, 2014, 23, 145-155.

[28] F. Yan, N. Feng, G. Zhang. *Crystengcomm*, 2014, 16(2), 214-222.

[29] V. H. Luan, H. N. Tien, S. H. Hur. *Journal of Colloid and Interface Science*, 2015, 437,181-186.

[30] W. Han, L. Ren, X. Qi, Y. Liu, X. Wei, Z. Huang, J. Zhong. *Applied Surface Science*, 2014, 299, 12-18.

[31] S G Zhang, L Wen, J L Li, F L Gao, X W Zhang, L H Li, G Q Li. *Journal of Physics D: Applied Physics*, 2014, (47), 495103.

[32] J.C. Lin, B.R. Huang, T.C. Lin. *Applied Surface Science*, 2014, 289, 384-387.

[33] K. Huang, Y.H. Li, S. Lin, C. Liang, H. Wang, C.X. Ye, Y.J. Wang, R. Zhang, D.Y. Fan, H.J. Yang, Y.G. Wang, M. Lei. *Power Technology*, 2014, 257, 113-119.

[34] H. N. Ashilyn, Y. H., M. M. Rusop, T. Tomoaki, H. A. Manaf. *Nanoscale research letters*, 2014,(9), 609-615.

[35] C. Wu, F. Li, Y. Zhang, T. Guo. *Carbon*, 2012, 50, 3622-2626.

[36] William S. Hummers, JR., Richard E. Offeman R. *J. Am. Chem. Soc.*, 1958, 80 (6), 1339-1139.

[37] Daniela C. Marcano, Dmitry V. Kosynkin, Jacob M. Berlin, Alexander Sinitskii, Zhengzong Sun, Alexander Slesarev, Lawrence B. Alemany, Wei Lu, and James M. Tour. *ACS NANO*, 2010, 4(8), 4806-4814.

[38] R. Lv, X. Wang, W. Lv, Y. Xu, Y. Ge, H. He, G. Li, X. Wu, X. Li and Q. Li. *Journal of Chemical Technology and Biotechnology*, 2015, 90(3), 550-558.

[39] X. Wang, R. Lv, K. Wang. *Journal of Materials Chemistry A*, 2014, 2, 8304-8313.

[40] Y. Al-Douri, M. Ameri, A. Bouhemado. Optik, 2014, 125, 6958-6961.

[41] Y. Al-Douri, H. Abid, H. Aourag, Mater. Chem. Phys., 2004, 87, 14-17.

[42] X. Zhou, T. Shi, H. Zhou. *Applied Surface Science*, 2012, 258, 6204-6211.

[43] C. Zhang, Z. Nan, Y. Xu. *Cryst.Eng.Comm.*, 2013, 15, 3022.

[44] B. Selin Tosun, Chelsea Pettit, Stephen A. Campbell, and Eray S. Aydil. *Applied Materials & Interface*, 2012, 4, 3676-3684.

[45] J. Shen, W. Huang, N. Li, M. Ye. *Ceramics International*, 41 (2015) 761-767.

[46] Akhavan, Omid. Graphene Nanomesh by ZnO Nanorod Photocatalysts. 2010, 7, 4174-4180.

[47] J. Jiang, M. Wang, L. Ma, Q. Chen, L. Guo. *International journal of hydrogen energy,* 2013, 38, 13077-13083.

[48] Ichimura, M., Furukawa, T.,Shirai, K. *Mater. Lett.* 1997, 33, 51-55.

[49] Shamir, J., Larach, S. Spectrochim. Acta, Part A 1971, 27, 2105-2108.

[50] Y. C. Zhang, W. W. Chen, and X. Y. Hu.*Crystal Growth & Design*, 2007, 7(3), 581.

[51] Gaurav Singh, Anshul Choudhary, D. Haranath, Amish G. Joshi, Nahar Singh, Sykhvir Singh, Renu Pasricha. *Carbon*, 2012, 50, 385-394.

[52] Z. Wu, L. Chen, C. Xing, D. Jiang, J. Xie and M. Chen, *Dalton Transactions*, 2013, 42, 12980-12988.

[53] J. Cao, B. Xu, H. Lin, B. Luo and S. Chen, *Dalton Trans.*, 2012, 41, 11482-11490.

[54] P. Gao, J. Liu, S. Lee, T. Zhang and D. D. Sun, *J. Mater. Chem.*, 2012, 22, 2292-2298.

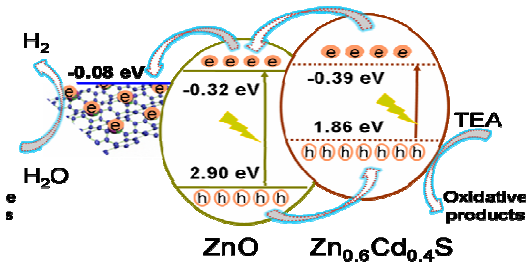

The synthesis of ZnO-core/$Zn_xCd_{1-x}S$-shell nanorods grown vertically on RGO sheets and important roles played by $Zn_xCd_{1-x}S$ on photocatalytic activity are described.